SCIENCE CHINA
Information Sciences

• RESEARCH PAPER •

November 2024, Vol. 67, Iss. 11, 212401:1–212401:7
https://doi.org/10.1007/s11432-023-3959-6

Artificial afferent neurons based on the metal-insulator transition of VO_2

Jiayao CHEN[1†], Lei YIN[1†], Yue WANG[1,2], Haolin WANG[1], Dongke LI[1,2*], Deren YANG[1,2] & Xiaodong PI[1,2*]

[1] *State Key Laboratory of Silicon and Advanced Semiconductor Materials & School of Materials Science and Engineering, Zhejiang University, Hangzhou 310027, China;*
[2] *Institute of Advanced Semiconductors & Zhejiang Provincial Key Laboratory of Power Semiconductor Materials and Devices, ZJU-Hangzhou Global Scientific and Technological Innovation Centre, Zhejiang University, Hangzhou 311215, China*

Received 9 September 2023/Revised 9 November 2023/Accepted 20 February 2024/Published online 12 October 2024

Abstract Neuromorphic computing offers significant advantages in addressing data redundancy and enhancing system energy efficiency. Although extensive research has been conducted on pulsed neural networks and bionic sensors, the development of artificial electronic afferent neurons for low-energy information transfer remains limited. This study introduces an artificial afferent neuron comprising a vanadium dioxide (VO_2) device, capacitor and resistor. The VO_2 devices exhibit stable electrically induced metal-insulator transition (MIT). Leveraging the MIT of this device, we develop an artificial afferent neuron to transform constant or sinusoidal analog signals into pulsed voltage signals. The output frequency increases with the increase of the input voltage, mimicking the faster pulse outputs of biological afferent neurons in response to stronger stimuli.

Keywords vanadium dioxide, metal-insulator transition, artificial afferent neurons, pulsed voltage signal, output frequency

1 Introduction

Owing to advancements in neuromorphic computing and bionic sensing [1], bionic intelligent robots have gained considerable attention. Bionic intelligent robots are predominantly designed to emulate biological perceptual systems, featuring effective information processing and rapid responses. Biological perceptual systems are complex, efficient, fault-tolerant, consisting of sensory receptors, afferent neurons, and a cerebral cortex [2–4]. In recent years, pulsed neural networks have been extensively investigated to simulate the cerebral cortex [5–10]. Owing to their synaptic plasticity, resistive random access memories (RRAMs) [11], phase-change memories (PCMs) [12], ferroelectric field-effect transistors (FeFETs) [13,14] and semiconductor-nanocrystal transistors [15–18] are considered potentially key components in artificial pulsed neural networks. External stimuli such as light, sound, smell, and pressure are typically conveyed as continuous analog signals, differing from the pulsed signals required by the central nervous system. Therefore, artificial afferent neurons designed to convert continuous analog signals into pulsed signals are required to facilitate information transfer between bionic sensors and the pulsed neural network [19–21].

Kim et al. [22] designed a tactile sensing system that integrated pressure sensors, organic ring oscillators, and neurosynaptic transistors on a flexible substrate. The circular oscillator functioned similarly to biological afferent neurons, converting the voltage signal received from a pressure sensor into voltage pulses to drive synaptic devices and generate postsynaptic currents. However, the extensive use of metal-oxide-semiconductor field-effect transistor (MOSFET) circular oscillators in tactile sensing systems complicates circuit structures, limiting the application of electronic afferent neurons in high-density neuromorphic intelligence chips. Tan et al. [23] combined a ring oscillator, an edge detector, and a light-emitting diode

* Corresponding author (email: ldkest@zju.edu.cn, xdpi@zju.edu.cn)
† Chen J Y and Yin L have the same contribution to this work.

© Science China Press 2024

(LED) to develop an optoelectronic afferent neuron capable of emitting light pulses. The optoelectronic afferent neuron was then connected to an MXene-based pressure sensor and a neural synaptic device based on an ITO/ZnO/NSTO photomemristor, leading to the development of a tactile sensing system based on optoelectronic devices. Yu et al. [24] proposed an artificial afferent neuron activated through contact electrification at femtojoule energy levels. External mechanical actions were easily converted into voltage spikes using a triboelectric nanogenerator (TENG). The triboelectric potential generated by charge transfer during contact electrification activated postsynaptic transistors, enabling spatiotemporal recognition of displacements, pressures, and touch patterns. Moreover, the converted mechanical energy could be harnessed to achieve the self-powered operation of artificial sensory neurons, resulting in a significant reduction in energy consumption. However, these structures are exclusively applicable to piezoelectric sensors, which are not readily extended to resistive sensors. Zhang et al. [21] developed an electron-afferent neuron leveraging the properties of the electrogenic metal-insulator transition (MIT) of NbO_x to generate pulse output, thereby simplifying the circuit structure. However, the rather high MIT temperature of NbO_x (1080 K) poses a challenge for the future development of low-power-driven neural devices.

In this study, we fabricate a VO_2 film with stable MIT. The switching performance of VO_2 surpasses that of NbO_2, demonstrating a faster switching speed and lower energy consumption. Notably, the simulated Mott transition occurs 100 times faster in VO_2 than in NbO_2. The corresponding energy consumption in VO_2 is approximately 16% of that in NbO_2 [25]. Consequently, these findings show promise for the development of future low-power-driven neural devices. The VO_2 film is employed to fabricate VO_2 devices with horizontal structures. These VO_2 devices exhibit electrically induced MIT under a low driving voltage, bidirectional Mott transitions, high uniformity and good endurance. An artificial afferent neuron with a simple circuit structure comprising a VO_2 device, capacitor, and resistor is then fabricated. This configuration enables the transformation of continuous analog signals into pulsed voltage signals. Notably, the output frequency increases with the increase of input voltages. This behavior faithfully mimics the phenomenon observed in biological afferent neurons, where stronger stimuli leads to faster pulse outputs. Our VO_2-based artificial afferent neuron offers a promising option for the development of low-power and highly integrated artificial impulse neural networks.

2 Experimental section

The top Si layer of the SOI wafer was first removed via ICP etching to obtain a SiO_2/Si substrate. Photolithography was employed to determine the pattern of the VO_x film on the SiO_2/Si substrate. The VO_x films were deposited at a fixed oxygen partial pressure of 5% using magnetron sputtering. The photoresist was subsequently removed via a lift-off process to obtain VO_x strips with dimensions of 20 μm × 45 μm. The VO_x strips on the SiO_2/Si substrate underwent annealing at 500°C for 120 min to promote the crystallization of VO_x into VO_2. Photolithography was repeated to define the patterns of the electrodes on the VO_2 strips. Electrodes consisting of 5 nm Ni and 250 nm Au were prepared using magnetron sputtering. Finally, the photoresist was removed using a lift-off process, resulting in VO_2 devices with a horizontal structure. Scanning electron microscopy (SEM, Gemini500), atomic force microscopy (AFM, Multimode-8), and Raman spectroscopy (Senterra) with a 532 nm laser were employed to examine the microstructures of the VO_2 films and devices. Electrical characterization was performed using a semiconductor parameter analyzer (FS480, PDA Co. Ltd.).

3 Results and discussion

3.1 MIT of VO_2

Figures 1(a)–(c) show the temperature-dependent resistances of the VO_2 films with different deposition times. The thicknesses of the VO_2 films under the deposition times of 300, 600, and 1200 s are approximately 113, 166, and 255 nm, respectively. The resistance curves indicate a clear hysteresis phenomenon owing to the latent thermal properties of VO_2. All VO_2 films exhibit temperature-dependent resistance changes greater than three orders of magnitude. The transition temperature of the MIT ($T_{\rm MIT}$) for the VO_2 films is determined by calculating the first-order derivative of the logarithm of the resistance given by the heating and cooling curves with respect to the temperature, as shown in Figures 1(d)–(f). The

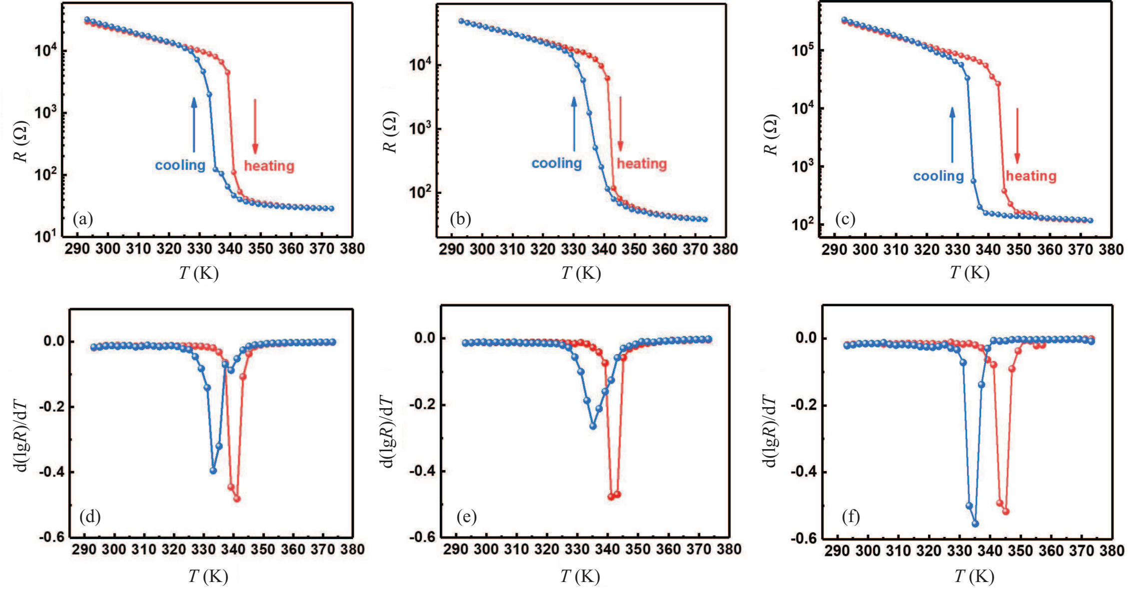

Figure 1 (Color online) Resistance-temperature (R-T) plots for VO_2 films with deposition times of (a) 300 s, (b) 600 s, and (c) 1200 s. Corresponding ($\frac{d(\lg R)}{dT}$-T) plots for VO_2 films with deposition times of (d) 300 s, (e) 600 s, and (f) 1200 s.

Table 1 $T_{\rm MIT}$ of VO_2 films with varying thicknesses during heating and cooling

Deposition time of VO_2 (s)	Thickness of VO_2 (nm)	$T_{\rm MIT}$ (heating) (K)	$T_{\rm MIT}$ (cooling) (K)
300	113	341	333
600	166	341	335
1200	255	345	335

$T_{\rm MIT}$ values of the VO_2 films with varying thicknesses during heating and cooling are listed in Table 1. The $T_{\rm MIT}$ of the VO_2 films is close to that of bulk VO_2 (341 K), indicating the high uniformity and excellent performance of the deposited VO_2 films [26].

3.2 Preparation and characterization of VO_2 devices with horizontal structure

The horizontal structure of the VO_2 device is shown in Figure 2(a). Figure 2(b) shows an optical image of a typical VO_2 device, showcasing the precise alignment of the electrodes with the VO_2 film. The channel between the electrodes measures 2.5 μm in length and 20 μm in width. The surfaces of the electrodes are smooth and flat without any photoresist residue. The SEM image in Figure 2(c) reveals the uniform grain size of the VO_2 film with a deposition time of 300 s. Furthermore, the inset in Figure 2(c) shows a high-resolution SEM image of the VO_2 film, indicating the absence of macroscopic defects, such as agglomeration or pinholes. The smooth surface of the VO_2 film (roughness of ∼0.5 nm) is confirmed by AFM (Figure 2(d)). The cross-sectional SEM image in Figure 2(e) reveals a smooth and abrupt interface between the VO_2 film and the Si/SiO_2 substrate. Figure 2(f) shows the characteristic peaks in the Raman spectrum of the device, where clear VO_2-related peaks indicate the high crystallinity of the VO_2 film.

To characterize the electrically induced MIT of the VO_2 device, the I-V characteristic of the device is tested in DC mode, scanning from −10 to 10 V, as shown in Figure 3(a). Following the forming process, the VO_2 device exhibits stable electrically induced MIT behavior under both positive and negative voltages, and the absolute values of the transition voltages are approximately equal. The absolute value of the threshold voltage ($V_{\rm TH}$) is ∼3.0 V, whereas the absolute value of the hold voltage (V_H) is ∼1.4 V. The resistance value of the device in the metallic state (LRS) is approximately 530 Ω at a voltage of 1.6 V. Figure 3(b) shows the I-V plot of the current sweep after forming. Initially, as the current increases from 0 to 110 μA, the voltage of the device increases linearly. The voltage subsequently exhibits a super-linear increase, indicating an increase in the temperature of VO_2. When the voltage reaches 3.0 V, the device undergoes an MIT. The VO_2 film instantaneously changes from the insulating state to the metallic state. Metallic VO_2 subsequently experiences a decrease in resistance as the current increases owing to Joule heating, resulting in a reduction in the voltage. When the current decreases from 200 to

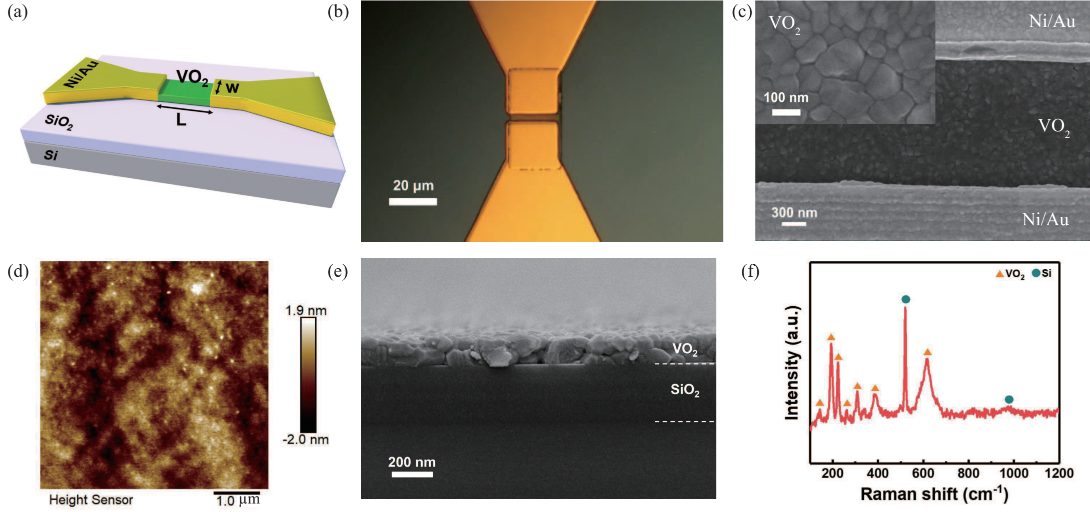

Figure 2 (Color online) (a) Schematic and (b) optical image of the VO_2 devices with a horizontal structure. (c) SEM and (d) AFM images of the VO_2 surface. (e) Cross-sectional SEM image and (f) Raman spectrum of the VO_2 film.

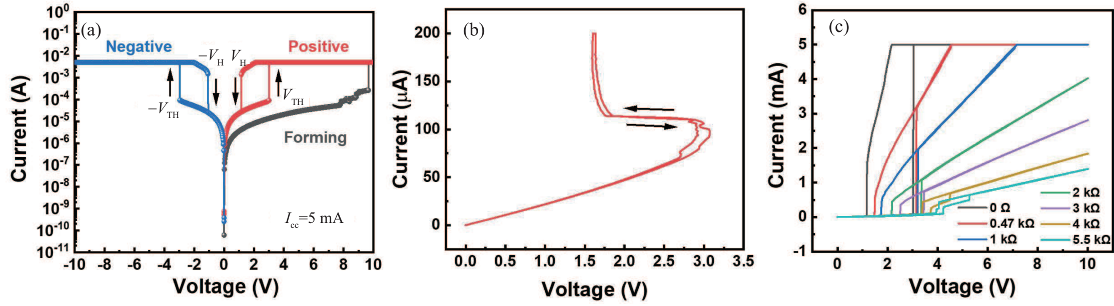

Figure 3 (Color online) (a) Forward and reverse DC operation of the VO_2 device under a voltage sweep; (b) DC operation of the VO_2 device under a current sweep; (c) DC operation of the VO_2 device in series with resistors of different values.

0 μA, the resistance of the device increases as the current decreases. When the voltage reaches 1.7 V, the VO_2 film undergoes an MIT from the metallic state to the insulating state. This transition causes a sudden increase in the resistance, leading to an abrupt increase in the voltage across the VO_2 film. The critical current for the MIT transition of the device is approximately 110 μA with a window of 3 μA. This narrow window suggests that the transition temperatures between the insulating and metallic states of the VO_2 device are similar [27]. Figure 3(c) shows the I-V plot when the VO_2 device is connected in series with different resistors. As the resistance of the series resistor increases, both $V_{\rm TH}$ and V_H increase. This phenomenon can be attributed to the voltage applied across the resistor and VO_2 device. As the resistance of the resistor increases, the voltage applied across the VO_2 device decreases, necessitating a higher total voltage to achieve the desired $V_{\rm TH}$ across the VO_2 device.

3.3 Fabrication and characterization of artificial afferent neurons

In biological sensory systems, afferent neurons are primarily responsible for converting analog signals received from sensory receptors, such as external images, sounds, and temperatures, into pulse signals required for brain processing [28,29]. In this study, an electronic afferent neuron is fabricated by combining a VO_2 device with a capacitor and resistor. This circuit is illustrated in Figure 4(a). The electronic afferent neuron is formed by connecting the VO_2 device in parallel with a capacitor of capacitance C_i, and then in series with a resistor of resistance R_S. When the voltage ($V_{\rm IN}$) of the input signal exceeds a certain value, the ungrounded end of the VO_2 device outputs a pulse signal with a certain frequency ($V_{\rm OUT}$).

The capacitance of the entire circuit is given by $C = C_i + C_{\rm par}$, where $C_{\rm par}$ is the parasitic capacitance, and $R_{\rm met} \ll R_S \ll R_{\rm ins}$, where $R_{\rm ins}$ and $R_{\rm met}$ represent the insulating and metallic state resistances of the VO_2 device, respectively. Because $R_{\rm ins}C \gg R_SC$, when $V_{\rm IN}$ is applied to the input terminal, the

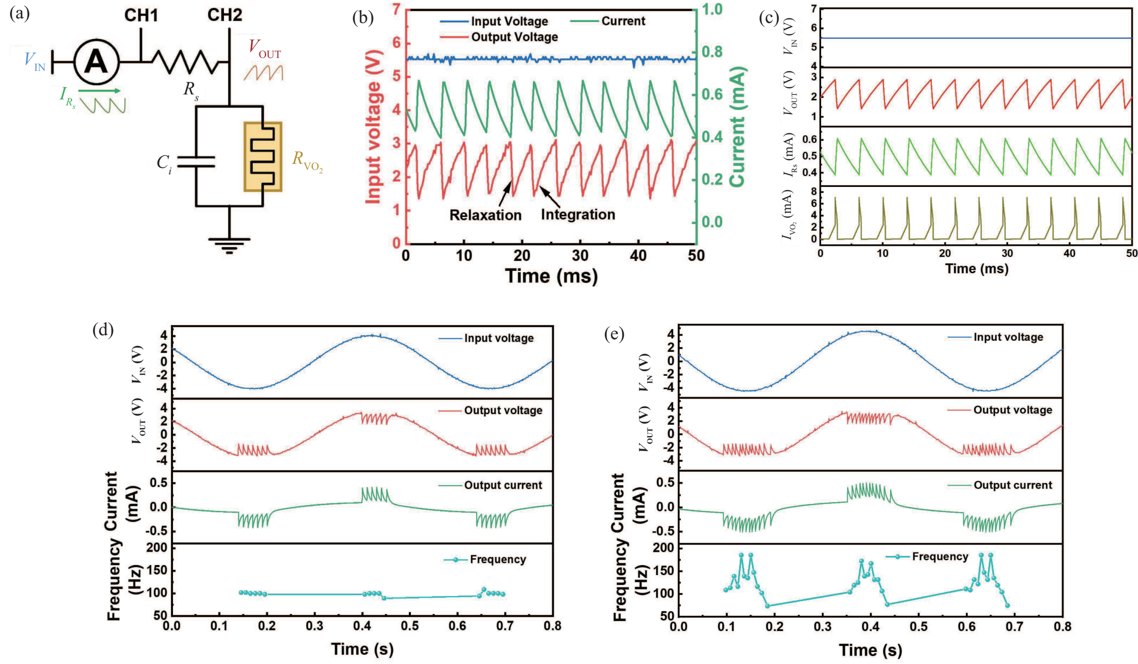

Figure 4 (Color online) (a) Circuit diagram of the artificial afferent neuron. (b) Oscillatory behavior of the artificial afferent neuron. (c) Oscillatory behavior of the simulated afferent neuron. Frequency response for sinusoidal input signals with amplitudes of (d) 4.0 V and (e) 4.5 V.

capacitor undergoes a charging process. During the charging process, the voltage across the capacitor $V_{\rm OUT}$ increases continuously until it exceeds $V_{\rm TH}$, at which point the VO_2 film undergoes MIT owing to Joule heating. At this stage, the resistance decreases from $R_{\rm ins}$ to $R_{\rm met}$. Since $R_{\rm met}C \ll R_SC$, the MIT transition leads to the discharge of the capacitance C. Consequently, the net charge of the capacitor decreases. $V_{\rm OUT}$ also gradually decreases until it becomes lower than V_H. When the Joule heating of the VO_2 device is insufficient to maintain the metallic state, VO_2 transitions from the metallic state to the insulating state, causing the resistance of VO_2 to return to $R_{\rm ins}$. Subsequently, the MIT is accompanied by repeated charging and discharging of the capacitor, resulting in periodic $V_{\rm OUT}$.

To achieve the oscillation output of the circuit, the electronic afferent neuron operates with R_S at 6.7 kΩ, $V_{\rm IN}$ at 5.5 V, and C_i at 1 μF, following the principles of VO_2-based relaxation oscillators [30]. As shown in Figure 4(b), the variation in $V_{\rm OUT}$ directly opposes the trend of the current variation, switching back and forth between V_H and $V_{\rm TH}$. The charging time for $V_{\rm OUT}$ to change from V_H to $V_{\rm TH}$ is defined as the integration time, while the discharge time required for $V_{\rm OUT}$ to change from $V_{\rm TH}$ to V_H is defined as the relaxation time. However, the current $I_{\rm VO_2}$ through the VO_2 device cannot be determined because of the inherent constraints of the test conditions. To obtain $I_{\rm VO_2}$, the output characteristics of the oscillation circuit are simulated using LT-Spice [30]. The simulated results for $V_{\rm OUT}$, $I_{\rm VO_2}$, and the current I_{R_s} flowing through R_S are shown in Figure 4(c). The simulated $V_{\rm OUT}$ and I_{R_s} values align well with the measured results shown in Figure 4(b). Moreover, $I_{\rm VO_2}$ exhibits oscillatory behavior, showing a linear increase during capacitor charging and a decline during capacitor discharging.

The VO_2 afferent neurons are further investigated under a sinusoidal voltage signal $V_{\rm IN}$. As shown in Figures 4(d) and (e), the second and third rows present the temporal variations of $V_{\rm OUT}$ and I_{R_s}, while the fourth row shows the frequency calculated from the output signal. When the input signal amplitude is 4.0 V (Figure 4(d)), the output frequencies of the afferent neurons are fixed at approximately 100 Hz. Furthermore, when the input signal is increased to 4.5 V (Figure 4(e)), the output frequencies also increase accordingly. This behavior faithfully mimics the phenomenon in which biological afferent neurons exhibit faster pulse outputs under stronger stimuli.

In addition to the MIT relaxation time, the oscillation frequency of the VO_2 afferent neurons is primarily determined by the charging rate of the capacitor. Consequently, the limit of the oscillation frequency primarily depends on the parasitic capacitance of the circuit [31]. The parasitic capacitance of the test circuit is determined by reducing the external capacitance of the VO_2 device until the oscillation fre-

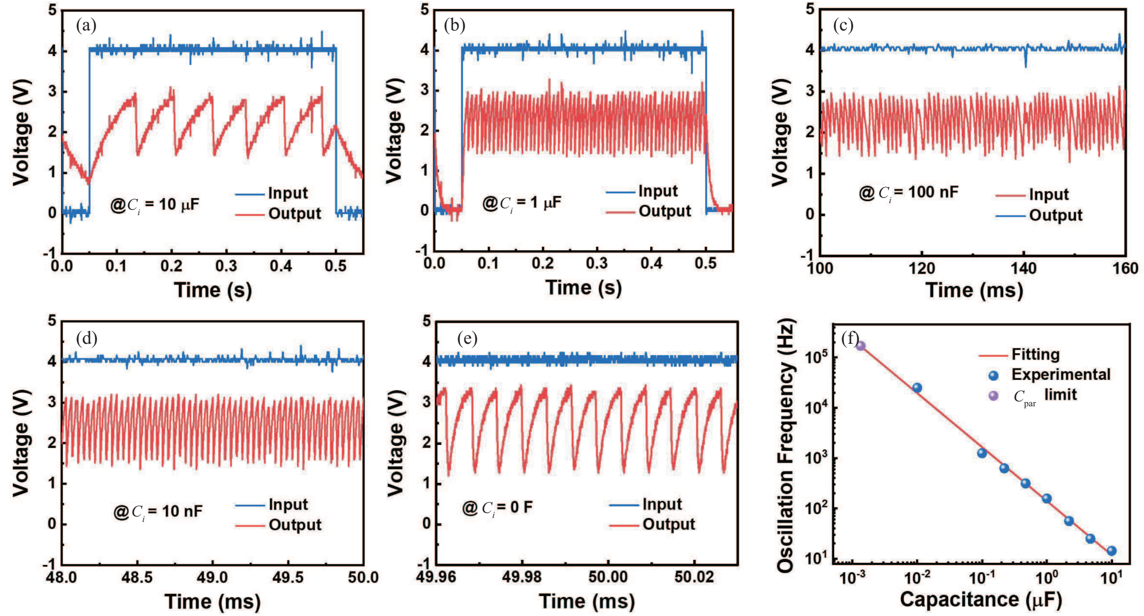

Figure 5 (Color online) Oscillation curves of the artificial afferent neurons at $V_{\rm IN}$ = 4 V with different capacitances of external parallel capacitors: (a) C_i = 10 μF, (b) C_i = 1 μF, (c) C_i = 100 nF, (d) C_i = 10 nF, and (e) C_i = 0 F. (f) Relationship between the oscillation frequency and the capacitance.

quency reaches its maximum value. Figures 5(a)–(e) show the oscillatory curves of the artificial afferent neurons versus the oscillation frequency of the circuit for different external capacitances. Figure 5(f) shows the linear relationship between the logarithm of the oscillation frequency and the logarithm of the capacitance, indicating that the oscillation frequency is inversely proportional to the capacitance. Figure 5(e) shows that the output oscillation frequency reaches its maximum value at 0.17 MHz when C_i = 0. By extrapolating the linearly fitted line in Figure 5(f), it is found that the parasitic capacitance of the entire circuit is 1.1 nF, which closely aligns with the reported value of parasitic capacitance in a circuit with a similar structure [30]. When constructing an electronic afferent neuron, appropriate capacitors should be selected to match the oscillation frequency of the afferent neuron with the maximum sampling frequency of the testing system.

4 Conclusion

In summary, we successfully prepared patterned VO_2 thin films using lithography, sputtering, lift-off, and annealing processes and subsequently fabricated VO_2 devices with a horizontal structure. The VO_2 films exhibit a stable transition between the metallic and insulating states within a narrow temperature range of 333–345 K. The VO_2 devices exhibit a stable electrically induced MIT under both positive and negative voltages. Moreover, the absolute values of the transition voltages are approximately equal. Finally, an artificial afferent neuron comprising a VO_2 device, capacitor, and resistor is designed to transform constant or sinusoidal analog signals into pulsed voltage signals under suitable $V_{\rm IN}$ and R_S. Furthermore, the parasitic capacitance of the VO_2 artificial afferent neuron is examined. We hope that the current VO_2-based artificial afferent neuron may significantly contribute to signal transformation in artificial neural networks.

Acknowledgements This work was supported by National Natural Science Foundation of China (Grant Nos. U22A2075, 92364204, 91964107, U20A20209), National Natural Science Foundation of China for Innovative Research Groups (Grant No. 61721005), Fundamental Research Funds for the Central Universities (Grant No. 226-2022-00200), and Leading Innovative and Entrepreneur Team Introduction Program of Hangzhou (Grant No. TD2022012).

References

1 Zhang W, Gao B, Tang J, et al. Neuro-inspired computing chips. Nat Electron, 2020, 3: 371–382
2 Sivaramakrishnan S, Sterbing-D'Angelo S J, Filipovic B, et al. GABAA synapses shape neuronal responses to sound intensity in the inferior colliculus. J Neurosci, 2004, 24: 5031–5043
3 Ikeda R, Cha M, Ling J, et al. Merkel cells transduce and encode tactile stimuli to drive a β-afferent impulses. Cell, 2014, 157: 664–675

4 Jung Y H, Park B, Kim J U, et al. Bioinspired electronics for artificial sensory systems. Adv Mater, 2019, 31: 1803637
5 Li Y Y, Wang Y, Yang D R, et al. Recent progress on optoelectronic synaptic devices (in Chinese). Sci Sin Inform, 2020, 50: 892–912
6 Li Y Y, Wang Y, Yin L, et al. Silicon-based inorganic-organic hybrid optoelectronic synaptic devices simulating cross-modal learning. Sci China Inf Sci, 2021, 64: 162401
7 Li Y, Tang J, Gao B, et al. Oscillation neuron based on a low-variability threshold switching device for high-performance neuromorphic computing. J Semicond, 2021, 42: 064101
8 Sokolov A S, Abbas H, Abbas Y, et al. Towards engineering in memristors for emerging memory and neuromorphic computing: a review. J Semicond, 2021, 42: 013101
9 Liao F, Zhou F, Chai Y. Neuromorphic vision sensors: principle, progress and perspectives. J Semicond, 2021, 42: 013105
10 Huang H, Ge C, Liu Z, et al. Electrolyte-gated transistors for neuromorphic applications. J Semicond, 2021, 42: 013103
11 Barraud S, Ezzadeen M, Bosch D, et al. 3D RRAMs with gate-all-around stacked nanosheet transistors for in-memory-computing. In: Proceedings of the IEEE International Electron Devices Meeting (IEDM), San Francisco, 2020
12 Boybat I, Le Gallo M, Nandakumar S R, et al. Neuromorphic computing with multi-memristive synapses. Nat Commun, 2018, 9: 2514
13 Zhu J, Zhang T, Yang Y, et al. A comprehensive review on emerging artificial neuromorphic devices. Appl Phys Rev, 2020, 7: 011312
14 Soliman T, Muller F, Kirchner T, et al. Ultra-low power flexible precision FeFET based analog in-memory computing. In: Proceedings of the IEEE International Electron Devices Meeting (IEDM), San Francisco, 2020
15 Yin L, Han C, Zhang Q, et al. Synaptic silicon-nanocrystal phototransistors for neuromorphic computing. Nano Energy, 2019, 63: 103859
16 Zhu Y, Huang W, He Y, et al. Perovskite-enhanced silicon-nanocrystal optoelectronic synaptic devices for the simulation of biased and correlated random-walk learning. Research, 2020, 2020: 7538450
17 Wang Y, Zhu Y, Li Y, et al. Dual-modal optoelectronic synaptic devices with versatile synaptic plasticity. Adv Funct Mater, 2022, 32: 2107973
18 Wang Y, Wang K, Hu X, et al. Optogenetics-inspired fluorescent synaptic devices with nonvolatility. ACS Nano, 2023, 17: 3696–3704
19 Yoon J H, Wang Z, Kim K M, et al. An artificial nociceptor based on a diffusive memristor. Nat Commun, 2018, 9: 417
20 Wall P D, Gutnick M. Properties of afferent nerve impulses originating from a neuroma. Nature, 1974, 248: 740–743
21 Zhang X, Zhuo Y, Luo Q, et al. An artificial spiking afferent nerve based on Mott memristors for neurorobotics. Nat Commun, 2020, 11: 51
22 Kim Y, Chortos A, Xu W, et al. A bioinspired flexible organic artificial afferent nerve. Science, 2018, 360: 998–1003
23 Tan H, Tao Q, Pande I, et al. Tactile sensory coding and learning with bio-inspired optoelectronic spiking afferent nerves. Nat Commun, 2020, 11: 1369
24 Yu J, Gao G, Huang J, et al. Contact-electrification-activated artificial afferents at femtojoule energy. Nat Commun, 2021, 12: 1581
25 Yi W, Tsang K K, Lam S K, et al. Biological plausibility and stochasticity in scalable VO_2 active memristor neurons. Nat Commun, 2018, 9: 4661
26 Zhang Y, Xiong W, Chen W, et al. Recent progress on vanadium dioxide nanostructures and devices: fabrication, properties, applications and perspectives. Nanomaterials, 2021, 11: 338
27 Bohaichuk S M, Kumar S, Pitner G, et al. Fast spiking of a Mott VO_2-carbon nanotube composite device. Nano Lett, 2019, 19: 6751–6755
28 Wang M, Luo Y, Wang T, et al. Artificial skin perception. Adv Mater, 2021, 33: 2003014
29 Wan C, Cai P, Wang M, et al. Artificial sensory memory. Adv Mater, 2020, 32: 1902434
30 Corti E, Gotsmann B, Moselund K, et al. Scaled resistively-coupled VO_2 oscillators for neuromorphic computing. Solid-State Electron, 2020, 168: 107729
31 Maffezzoni P, Daniel L, Shukla N, et al. Modeling and simulation of vanadium dioxide relaxation oscillators. IEEE Trans Circ Syst I, 2015, 62: 2207–2215